Energy Storage Materials 40 (2021) 209–218

Contents lists available at ScienceDirect

Energy Storage Materials

journal homepage: www.elsevier.com/locate/ensm

Sodium vanadate/PEDOT nanocables rich with oxygen vacancies for high energy conversion efficiency zinc ion batteries

Wenchao Bi[a,b,c], Guohua Gao[a,*], Guangming Wu[a,*], M. Atif[d,e], MS AlSalhi[d,e], Guozhong Cao[c,*]

[a] Shanghai Key Laboratory of Special Artificial Microstructure Materials and Technology, School of Physics Science and Engineering, Tongji University, Shanghai 200092, China

[b] Departments of Physics, College of Science, University of Shanghai for Science and Technology, Shanghai 200093, China

[c] Department of Materials Science and Engineering, University of Washington, Seattle, WA 98195-2120, United States

[d] Research Chair on Laser Diagnosis of Cancers, Department of Physics and Astronomy, College of Science, King Saud University, 11451, Riyadh, Saudi Arabia

[e] Department of Physics and Astronomy, College of Science, King Saud University, 11451, Riyadh, Saudi Arabia

ARTICLE INFO

Keywords:
Aqueous zinc-ion batteries
Cathodes
Oxygen vacancies
Sodium vanadate
PEDOT

ABSTRACT

Aqueous zinc-ion batteries (ZIBs) have received an increasing attention for large-scale energy storage due to its low cost and high safety. However, the sluggish kinetics stemming from the limited Zn^{2+} diffusion pathway and the strong electrostatic interaction between Zn^{2+} and the anion sublattice in the host crystal are great challenges for high-efficient Zn^{2+} storage. To circumvent these hurdles, bridge-oxygen sited oxygen vacancies are introduced in sodium vanadate $Na_{0.76}V_6O_{15}$ (NVO) through the *in-situ* polymerization of 3,4-ethylenedioxythiophene. In the resultant oxygen-vacancy rich NVO/poly(3,4-ethylenedioxythiophene) (PEDOT) nanocables (noted as $Vo^{\cdot\cdot}$-PNVO), the interplanar space is enlarged and the electrostatic interaction is weakened by the introduction of "oxygen vacancies" for fast reversible Zn^{2+} diffusion and intercalation. The conductive PEDOT coating also provides desired electronic conductivity and improves the structural integrity of NVO. Consequently, $Vo^{\cdot\cdot}$-PNVO based ZIBs exhibit an enhanced specific capacity (355 mA h g^{-1} at 50 mA g^{-1}), significantly enhanced energy conversion efficiency (>80%), and long lifespan (99% of the initial capacity remained after 2600 cycles).

1. Introduction

Aqueous rechargeable batteries have emerged as promising alternative technology for large-scale energy storage due to their inherent safety, affordable cost and feasible fabrication [1,2]. Zn^{2+} possess high theoretical capacity (820 mA h g^{-1}), low redox potential (−0.76 V vs standard hydrogen electrode) and excellent stability in water, leading to increasing research works on rechargeable aqueous zinc-ion batteries (ZIBs). [2,3] Until now, various cathode materials have been studied for high-performance aqueous ZIBs, such as manganese-based materials [4–6], vanadium-based composites [7,8], Prussian blue and its analogues [9], and transition-metal dichalcogenides [10,11]. Among them, vanadium-based materials can deliver high theoretical specific capacity (up to 588 mA h g^{-1}) and excellent electrochemical stability owing to their multiple valence states and open-framework structure [12,13]. Pure vanadium oxides, such as V_2O_5 [14] and VO_2 [15], usually show poor rate performance and cycling stability because their moderate sluggish ionic diffusion kinetics would lead to structure degradation during the repeated intercalation/deintercalation process of Zn^{2+}. Introducing metal ions (Na^+, K^+, Mg^{2+}. Al^{3+}) [16–19] or/and structural water molecules [20] between [V-O] polyhedron layers to expand interlayer space is an effective strategy to enhance Zn^{2+} diffusion kinetics. Metal vanadate, such as sodium vanadate [7,21] and potassium vanadate [18] with a layer or tunnel structure have also received much attention as the inserted metal ions can improve the structural stability. It has been reported that 2D layered sodium vanadate, such as $Na_5V_{12}O_{32}$ and $HNaV_6O_{16}\bullet 4H_2O$, can deliver high ion diffusion coefficients (from 10^{-10} to 6×10^{-10} cm^2 s^{-1}) and high capacities (281 and 304 mA h g^{-1} at 500 mA g^{-1}, respectively) [21], because a layer structure provides effective pathway for Zn^{2+} diffusion. Unfortunately, the structural destroy and capacity fading also accompanied, i.e., only 71% capacity retention after 2000 cycles was retained for $Na_5V_{12}O_{32}$ [21]. Sodium vanadate with a 3D rigid tunnel structure, such as $Na_{0.76}V_6O_{15}$ [21](notes as NVO), can effectively alleviate the structure collapse and exhibit reversible insertion/extraction of Zn^{2+}. However, the tunneled NVO shows an unsatisfactory capacity (135 mA h g^{-1} at 0.5 A g^{-1}) because the tunnel structure with smaller lattice space provide less effective diffusion paths for Zn^{2+} than the layer structure [21]. Thus, more efforts are necessary to achieve a better fundamental understanding and to modify the tunnel sodium vanadate as high-capacity and superior-stability cathode materials for ZIBs.

* Corresponding authors.
E-mail addresses: gao@tongji.edu.cn (G. Gao), wugm@tongji.edu.cn (G. Wu), gzcao@u.washington.edu (G. Cao).

https://doi.org/10.1016/j.ensm.2021.05.003
Received 6 January 2021; Received in revised form 11 April 2021; Accepted 3 May 2021
Available online 9 May 2021

To circumvent the challenges discussed above, vanadium-based materials are often composited with conductive materials, such as carbon materials [22–24] and conductive polymers [25,26] to improve the electrochemical kinetics and cycling capability of ZIBs with their high electronic conductivity. In addition, defect engineering, especially oxygen vacancies, are introduced as an effective strategy to modify the crystalline structure of materials and reduce the activation energy of Zn^{2+} insertion and diffusion [15,23,27]. Thus, the reaction and transport kinetics are intrinsically improved, and Zn^{2+} storage capability is significantly enhanced by oxygen vacancies [15,23].

In this work, oxygen vacancies in sodium vanadate, $Na_{0.76}V_6O_{15}$ nanobelts (NVO), were introduced through *in-situ* polymerization of poly(3,4ethylenedioxythiophene) (PEDOT) coating and studied for ZIBs. The resultant oxygen-vacancy rich NVO/PEDOT nanocables (noted as $Vo^{\cdot\cdot}$-PNVO) demonstrated a high capacity, much enhanced transport properties, and excellent cycling stability, attributing to: (1) enlarged interplanar space benefitting ion diffusion, (2) reduced polarization arising from the electrostatic interactions, (3) excellent electronic conductivity of PEDOT coating, and (4) enhanced mechanical integrity of NVO coated with conductive and stable PEDOT. Density functional theory (DFT) calculations are used to confirm the presence and site of oxygen vacancies.

2. Experimental section

2.1. Materials synthesis

2.1.1. Synthesis of $Na_{0.76}$ V_6O_{15} nanobelts (NVO)

0.5 g of commercial V_2O_5 powder was added into 50 mL of DI water and kept stirring at room temperature for 2 h to form solution A. Then, 1.0 g sodium dodecyl benzene sulfonate dispersed in 30 mL DI water by stirring was added in solution A. After stirring for another 2 h, the obtained orange suspension was transferred to 100 mL Teflon-lined stainless-steel autoclave and kept at 180 °C for 7 days. After solvent replacement with DI water and ethanol, and the sample was freeze dried in vacuum. Finally, the NVO was obtained after being heated in air at 450 °C for 3 h.

2.1.2. Synthesis of $Na_{0.76}V_6O_{15}$/PEDOT nanocables ($Vo^{\cdot\cdot}$-PNVO)

The obtained NVO was put in a vacuum environment with 0.5 mL HCl at room temperature for 1 h. Then, the sample was moved to a vacuum reactor with 0.1 mL 3, 4-ethylenedioxythiophene (EDOT) monomers and kept at 80 °C for 6 h. With EDOT monomers polymerized at the surface of NVO, $Vo^{\cdot\cdot}$-PNVO nanocables were obtained after further dried in air at 120 °C overnight.

2.2. Material characterizations

X-ray diffraction (XRD) with Bruker D8 Discover X-ray diffractometer and an ImS 2-D detection system (50 kV, 1000 mA) was used to characterize the crystalline phase of materials. The composition of samples was identified with Fourier-transform infrared (FTIR) spectra using a Bruker-TENSOR27 FTIR spectrometer from 1800 to 400 cm^{-1}, Raman spectra performing on a Jobin-Yvon HR800 Raman microscope ($\lambda = 514$ nm) recorded from 100 to 1800 cm^{-1}, and Thermogravimetric and differential scanning calorimetry (TG-DSC) measurements on SDT Q600 from 25 to 700 °C (10 °C min^{-1}, flowing air). Electron spin resonance (ESR) measurements were carried out on Bruker BioSpin GmbH. X-ray photoelectron spectra (XPS) were obtained by using a Thermo ESCALAB 250XiX spectrometer in the PHI-5,000C ESCA system with Mg Kα radiation ($h\nu$ = 1253.6 eV). The ratio of oxidation state was estimated from the corresponding peak area ratio. The morphologies and structures of materials were identified by field-emission scanning electron microscope (FE-SEM, S-4800) with an Energy-dispersive X-ray spectrometer (EDS), transmission electron microscopy and high-resolution transmission electron microscopy (TEM, HRTEM, JEOL-JEM2100) with Energy Dispersive X-ray spectrometry (EDS) element mapping analysis of High-Angle Annular Dark-Field Scanning Transmission Electron Microscopy (HADDF-STEM).

2.3. Electrochemical characterizations

Electrochemical performance of zinc ion batteries was tested using CR2032 coin-type cells fabricated in air, respectively. The corresponding electrolyte is 3 M zinc trifluoromethanesulfonate (98%, $Zn(CF_3SO_3)_2$) aqueous solution and 3 M $ZnSO_4$ aqueous solution for ZIBs, respectively. A glass fiber filter (Whatman, Grade GF/A) was chosen as the separator for ZIBs. Active material, conductive carbon and polyvinylidene fluoride (PVDF) were mixed in a mass ratio of 7: 2: 1 in N-methyl-2-pyrrolidone (NMP). Then, the obtained slurry was painted on the current collector (titanium foil) and heated at 100 °C in vacuum overnight. The mass loadings of the working electrodes are about 1.5 ~ 2 mg cm^{-2}. The electrochemical performance of the electrodes was tested by cyclic voltammetry (CV) and electrochemical impedance spectroscopy (EIS) measurements on CHI760e Shanghai Chenhua workstations. Galvanostatic charge/discharge (GCD) measurements were conducted with a multichannel battery testing system (LAND CT2001A). The working voltage of batteries was set from 0.3 to 1.5 V versus Zn^{2+}/Zn. Galvanostatic intermittent titration technique (GITT) was carried out at a current pulse of 50 mA g^{-1} for 10 min and a following relaxation time for 30 min in each step. The internal reaction resistance (RR) was calculated using the IR drop with the applied current density and the resistances at different steps. EIS measurements were tested with a frequency range of 100 kHz to 0.01 Hz.

2.4. Density functional theory (DFT) calculations

DFT was used to identify the possible sites of oxygen vacancies in NVO by using Vienna ab initio simulation package (VASP) [28]. The exchange and correlation energy functional were treated by the Perdew–Burke–Ernzerh of variant of the generalized gradient approximation (*GGA*) [29]. Interaction between ion and electrons was described with projector augmented wave pseudo potentials (PAW) [30,31] approach. The energy cutoff for the plane wave basis set was set as 500 eV, and the total energy was converged to 10^{-5} eV. Effective *U* parameter of 3.1 eV was used to describe the electronic structure of V [32]. The lattice parameters of NaV6O15 were optimized to be 15.85 Å × 3.68 Å × 10.41 Å with $\alpha = 90^{\circ}$, $\beta = 112^{\circ}$, $\gamma = 90^{\circ}$. K-points used for k-point sampling in irreducible region of the first Brillouin zone ensure the accuracy of the calculation within 1 meV.

3. Results and discussion

3.1. Composition and morphology of $Vo^{\cdot\cdot}$-PNVO

Oxygen vacancies in $Vo^{\cdot\cdot}$-PNVO nanocables were introduced with vapored polymerization method [33]. In brief, with NVO as oxidant, vapored EDOT *in-situ* oxidatively polymerized and chemically connected with NVO via the positive S cations in PEDOT and the negative O anions in NVO, forming a nanocable-structured $Vo^{\cdot\cdot}$-PNVO. Meanwhile, oxygen vacancies and accompanied V^{4+} were generated in $Vo^{\cdot\cdot}$-PNVO in the non-oxygen atmosphere.

The XRD patterns of both $Vo^{\cdot\cdot}$-PNVO and NVO demonstrate a pure $Na_{0.76}V_6O_{15}$ phase (JPDS No. 75-1653) in Fig. 1a. In this crystal structure, VO_6 octahedra connect the $[V_6O_{15}]_n$ layers by corner-shared oxygen atoms and form a tunnel structure (insert in Fig. 1a). Three distinctive peaks at $2\theta = 9.30^{\circ}$, 12.16° and 18.6° correspond to the (001), (200) and (−202) planes of $Na_{0.76}V_6O_{15}$, respectively. The relatively reduced peak intensity of $Vo^{\cdot\cdot}$-PNVO implies amorphous information which may be attributed to PEDOT and oxygen vacancies.

In the FTIR spectrum (Fig. 1b) of NVO, peaks at 493 and 553 cm^{-1} originate from the stretching vibration of chain-coordinated V–O_c bonds

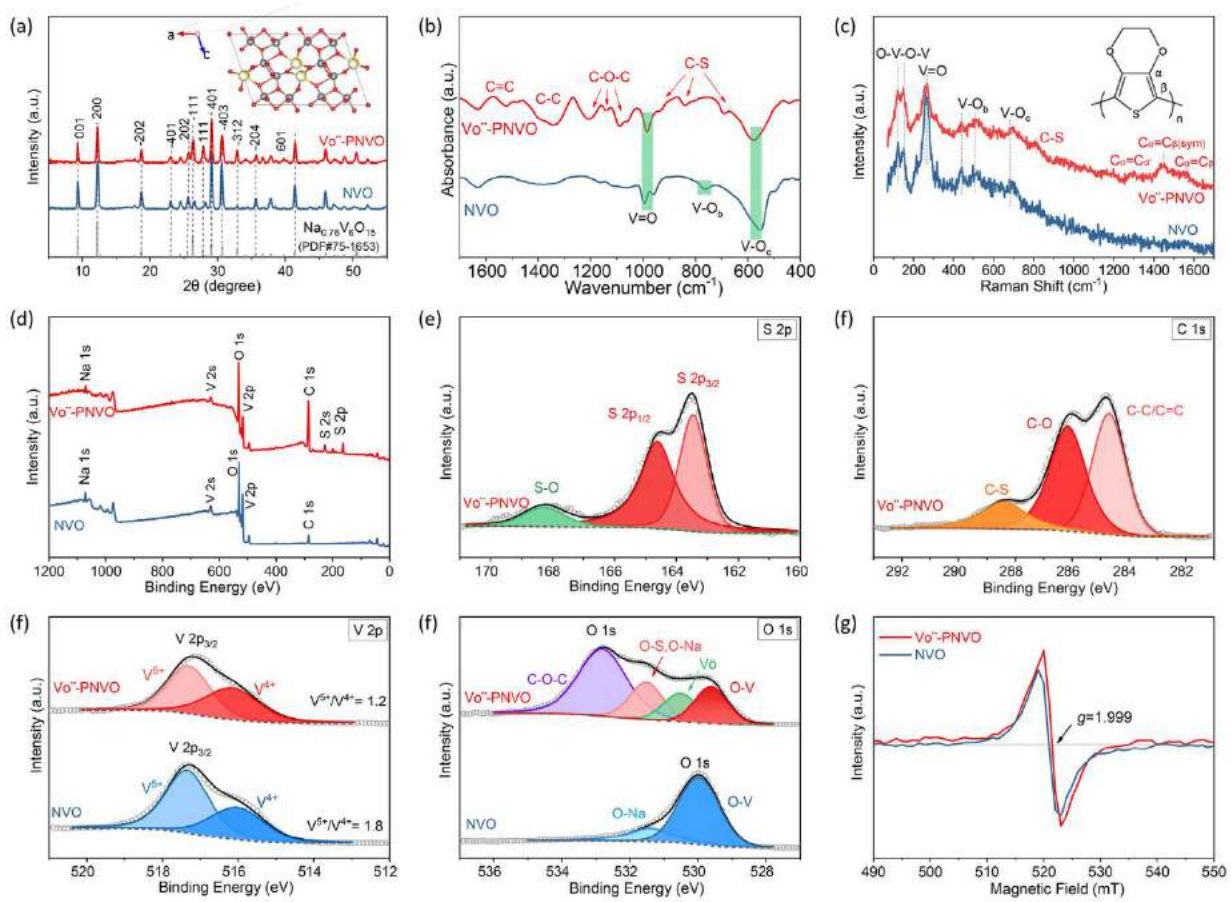

Fig. 1. Composition, bonding, and crystal structure characterization results of Vo¨-PNVO and NVO: (a) XRD patterns, (b) FTIR spectra, (c) Raman spectra, (d) Full survey XPS spectra, and high-resolution XPS spectra in (e) S 2p, (f) C 1 s, (g) V $2p_{3/2}$, and (h) O 1 s. (i) ESR spectra. A *g* factor of 1.999 and enhanced intensity suggest the existence of Vo¨ in Vo¨-PNVO.

[34]. The peak at 767 cm^{-1} is related to the symmetric stretching vibration of bridge-coordinated V–O_b bonds, and those located at 995 and 958 cm^{-1} are attributed to the stretching vibration of terminal V=O bonds[13]. Absorption bands at around 1377 and1631 cm^{-1} are caused by the vibration of Na–O bonds and O–H bonds from absorbed water, respectively [13,34]. In the spectrum of Vo¨-PNVO, apart from the characteristic peaks of NVO, the stretching vibration of C–S bonds (690, 839, 933 cm^{-1}), C–O–C bonds (1207, 1140, 1087 cm^{-1}), C–C and C=C bonds (1397, 1522 cm^{-1}) are observed, suggesting the formation of PEDOT in Vo¨-PNVO [35]. The peak of V–O_b bonds (767 cm^{-1}) vanishes, and only one peak for V=O bonds (984 cm^{-1}) is remained. Moreover, a blue shift in the peak of V–O_c bonds suggests the V–O_c bonds become stronger in Vo¨-PNVO. [13] These changes should relate to the oxygen vacancies and the connections between PEDOT (positive S) and NVO (negative terminal O), respectively (further explorations in following part) [36]. The above analysis indicates that Vo¨-PNVO remains its crystalline structure with tiny changes.

Raman spectra of Vo¨-PNVO and NVO were collected as complementary fingerprints to the FTIR spectra (Fig. 1c). Peaks located at 122 and 152 cm^{-1} come from the bending vibration of O–V–O–V bonds, which are related to the compressive deformation of lattice in tunnel-structured NVO [13,37]. Comparatively, a red shift of O–V–O–V peak (3 cm^{-1}) in Vo¨-PNVO suggests a weaker compression deformation [13]. As a result, a larger lattice space will be provided to facilitate the diffusion of Zn^{2+} in Vo¨-PNVO, which can be confirmed by the following IFFT of HRTEM images. The bending vibration of V=O bonds in Vo¨-PNVO becomes weak at 258 and 265 cm^{-1} due to the S–O connections with PEDOT [36], and the stretching signal of V–O_c bonds appears with a blue shift to 695 cm^{-1} [38], which is in accordance with FTIR analysis. The vibration of V–O_b bonds is slightly weakened at 440 and 516 cm^{-1} in Vo¨-PNVO [23], while it disappears in FTIR analysis. This can be explained that V–O_b bonds are partially weakened by oxygen vacancies as oxygen vacancies are generated at the interface of NVO and PEDOT and inner part retains its original valence states, similar to our precious work Vo¨-V_2O_5/polyaniline [33]. The formation of PEDOT is proved by the new bonds at 810, 1295, 1453, and 1560 cm^{-1}, which are assigned to the C–S, C_β–C_β, symmetric C_α=C_β(–O) and asymmetric C_α=C_β stretching modes, respectively. [25,38,39] Based on the FTIR and Raman spectra of Vo¨-PNVO, PEDOT anchored NVO at the terminal O, and oxygen vacancies are most likely to form at O_b site (further confirmed by following theoretical calculations). In this case, there would be an enlarged space for Zn^{2+} diffusion (to be further discussed). The mass of PEDOT accounts for 17% in Vo¨-PNVO, reflected by a mass loss and an exothermic peak at around 300 °C [40], as shown in TG-DSC results (Fig. S1).

Fig. 1d demonstrates the full survey XPS spectra of Vo¨-PNVO and NVO. Compared with NVO, two new peaks of S 2 s and S 2p are detected in Vo¨-PNVO, which are the characteristic peaks of PEDOT. The S 2p spectrum (Fig. 1e) can be deconvoluted into three peaks centered at 163.4, 164.6 and 168.3 eV, corresponding to S $2p_{3/2}$, S $2p_{1/2}$ and S-O bonds, respectively [35,41]. The C 1 s spectrum of Vo¨-PNVO in Fig. 1f is deconvoluted into three peaks of C–C/C=C, C–S, and C=O bonds in PEDOT [35,38,42], and the pure NVO without PEDOT only shows a weak signal of C 1 s spectrum (Fig. 1d). Fig. 1g displays asymmetric V $2p_{3/2}$

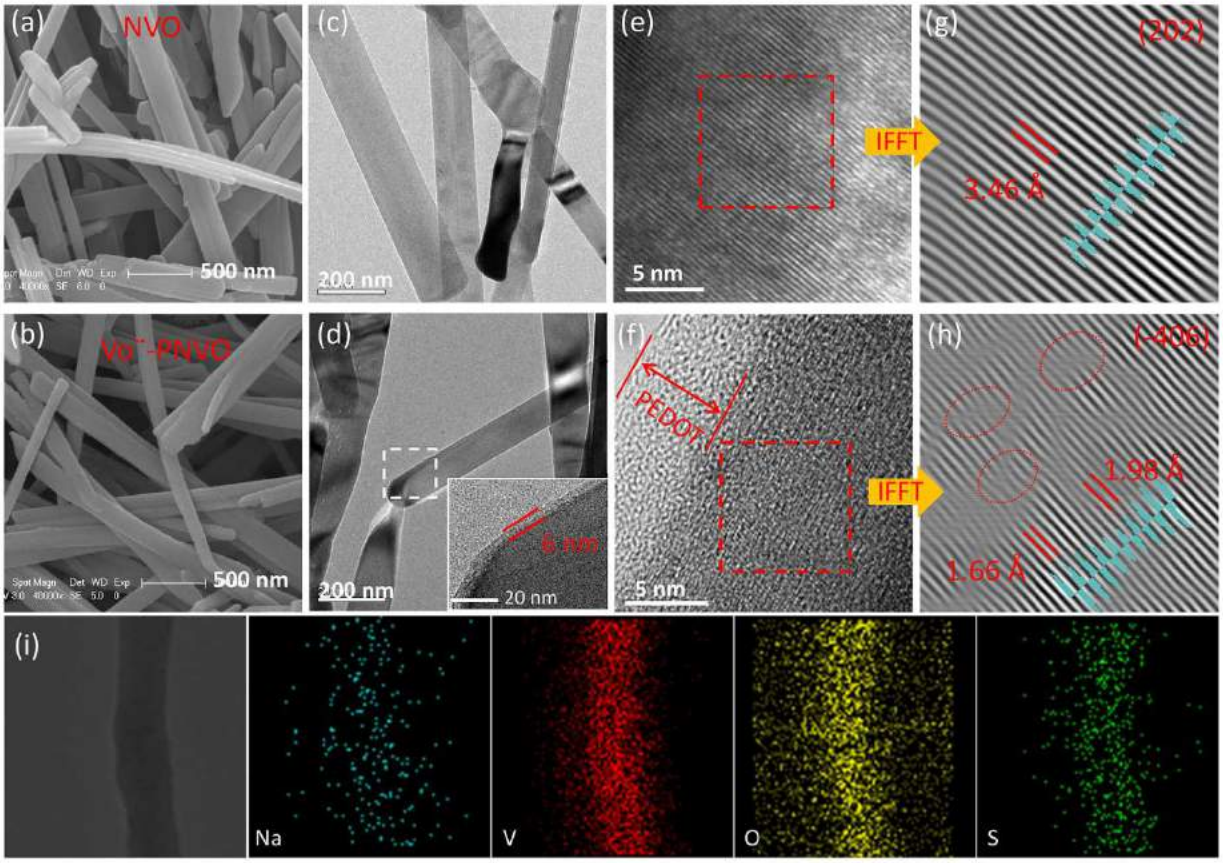

Fig. 2. (a and b) SEM images, (c and d) TEM images, (e and f) HRTEM images, (g and h) IFFT images and corresponding line profiles of the selected areas of NVO and Vo¨-PNVO. (i) TEM-EDS elemental mappings of Vo¨-PNVO.

spectra of Vo¨-PNVO and NVO. Calculated with the curve area ratio, the V^{5+}/V^{4+} ratio of Vo¨-PNVO (1.2) is lower than that of NVO (1.8), suggesting that a certain amount of V^{5+} species are reduced to V^{4+} when oxygen vacancies are generated in Vo¨-PNVO. For O 1 s spectrum, NVO shows peaks of O–V and O–Na bonds at 529.9 and 531.4 eV, respectively (Fig. 1h) [23]. In contrast, the O 1 s spectrum of Vo¨-PNVO is deconvoluted into four peaks at 529.6, 530.5, 531.5 and 532.8 eV, which correspond to the O–V bonds, oxygen vacancies, O–Na/O–S bonds and C–O bonds (thiophene ring) of PEDOT, respectively [23,27,43].

The bulk examination of oxygen vacancies was conducted by EPR measurements after above XPS surface characterizations. Oxygen vacancies as well as V^{4+} can be identified by EPR due to unpaired electrons [15]. As shown in Fig. 1i, both NVO and Vo¨-PNVO show characteristic EPR response at $g = 1.999$, and the peak intensity in Vo¨-PNVO is slightly higher than that of NVO. This is because extra oxygen vacancies accompanied with V^{4+} are generated in Vo¨-PNVO besides the original V^{4+} in NVO [15,23,38]. Considering the nanocable structure of Vo¨-PNVO, the slight difference in bulk analysis (EPR) and significant change in surface analysis (XPS) confirm the surface distribution of oxygen vacancies in Vo¨-PNVO. This surface distribution also agrees well with above XRD, FTIR and Raman analysis. Oxygen vacancies at the surface would facilitate the ion diffusion and electron transfer and suppress electrochemical polarization, improving the electrochemical rate performance and cycling stability of Vo¨-PNVO.

The SEM images (Fig. 2a and b), TEM images (Fig. 2c and d) show a nanobelt structure for NVO, while Vo¨-PNVO demonstrate a nanocable structure with a ~6 nm uniform coating. The uniform PEDOT coating is further confirmed by a homogeneous and broad distribution of S element, as shown in EDS elemental mappings of HADDF-STEM in Fig. 2i. The HRTEM image of NVO (Fig. 2e) and corresponding Inverse Fast Fourier Transform (IFFT) image (Fig. 2g) present perfect lattice fringes with an interplanar spacing of 3.46 Å, which is indexed to the (202) plane of NVO (JPDS No. 75-1653). Comparatively, Vo¨-PNVO show indistinct interface between PEDOT and NVO (Fig. 2f). This suggests the oxygen vacancies are induced in the near-surface layer of NVO, and it agrees well with the $V-O_b$ bond analysis based on FITR and Raman spectra. Moreover, dislocations (red circles) are observed in Vo¨-PNVO, and the corresponding interplanar spacing of (−406) plane is expanded from 1.66 Å to 1.98 Å (Fig. 2h). This is because oxygen vacancies cause the skewing of other atoms around and form dislocations in Vo¨-PNVO, and the accompanied V^{4+} with a bigger ionic radius (72 pm) also enlarge the interplanar distance than V^{5+} (68 pm), which is consist with XPS and EPR results. As a result, ion diffusion would be enhanced and the electrostatic interactions would be weakened to improve the rate performance and cycling stability of Vo¨-PNVO.

Based on above experimental analysis, the site of oxygen vacancies in NVO was further identified by DFT calculations. Different from orthorhombic V_2O_5 which consists of VO_5 pentahedrons, tunneled NVO consists of VO_6 octahedrons. As shown in Fig. 3a and b, VO_6 octahedrons connect each other through $V-O_b$ bonds and link layers with $V-O_c$ bonds. According to the crystalline symmetry, there are three possible sites in NVO: terminal O_v (Site 1), O_b (Site 2) and O_c (Site 3). The calculations suggest that the free energy of oxygen vacancy on Site 2 (−317.585 eV) is smaller than that on Site 1 (−317.268 eV) and Site 3 (−317.259 eV), as shown in Fig. 3b. This result suggests that oxygen vacancies are easier to form at O_b site, in agreement with the FTIR and Raman results. The $V-O_b$ bonds between layers are broken by oxygen vacancies, which can increase interplanar distance and reduce electrostatic interactions between Zn^{2+} and NVO, rendering fast Zn^{2+} diffusion and reversible Zn^{2+} intercalation in Vo¨-PNVO.

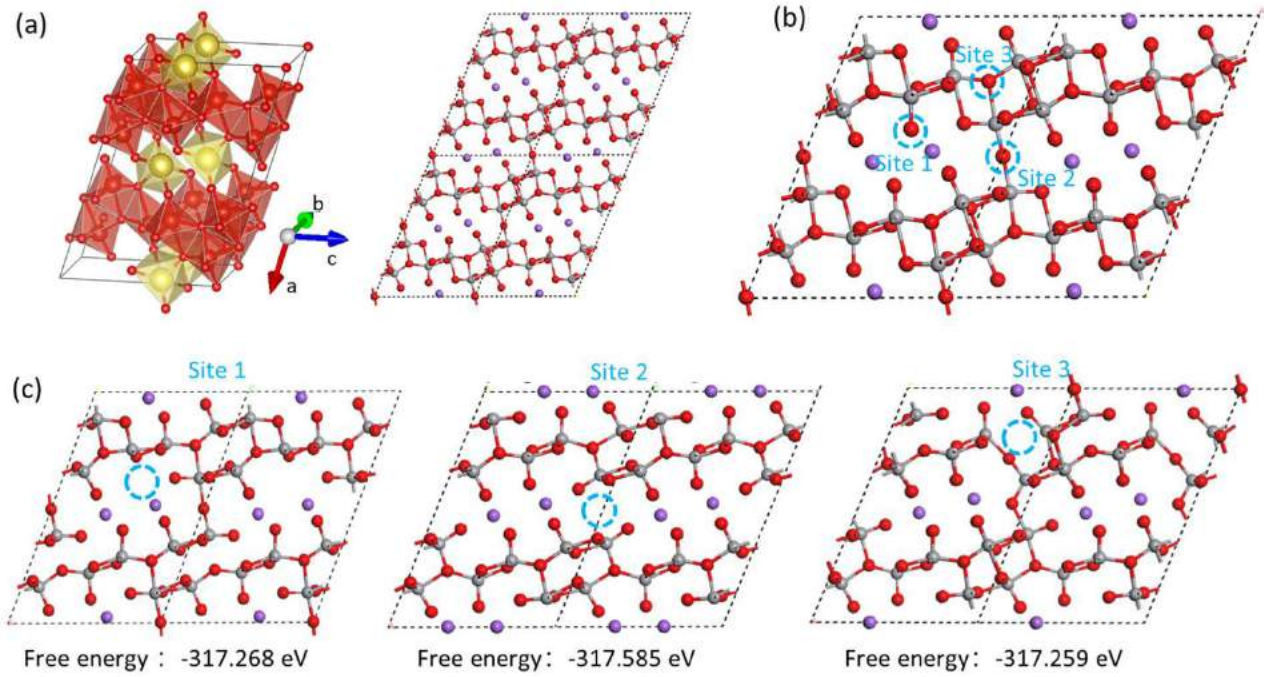

Fig. 3. (a) The crystal structure of NVO. (b) The possible sites for oxygen vacancies in NVO, and (c) corresponding calculated free energy. The smallest free energy on Site 2 suggests O_b site is the location of oxygen vacancies in Vo¨-PNVO.

3.2. Electrochemical characteristics and properties of Vo¨-PNVO

The electrochemical characteristics and properties of Vo¨-PNVO and NVO as cathode materials for ZIBs were evaluated by assembling coin cells with 3 M $Zn(CF_3SO_3)_2$ aqueous solution as electrolyte. In the cyclic voltammetry (CV) curves of NVO at 0.1 mV s^{-1} (Fig S2a), there are three pairs of redox peaks centered at 1.1/1.28 V, 0.52/0.85 and 0.42/0.75 in the first cycle, which correspond to V^{5+}/V^{4+} and V^{4+}/V^{3+}, respectively [19,37,38]. These redox pairs move to 1.1/1.33, 0.50/0.88 and 0.41/0.79 V in the subsequent 3rd and 4th cycles, respectively. The gradually enlarged voltage gap in redox pairs and reduced CV curve area suggest serious polarization and capacity decay in NVO. This is related to irreversible reactions, namely "dead Zn^{2+}", happened in the Zn^{2+} insertion/extraction processes, similar in $Na_{0.33}V_2O_5$ [44]. In contrast, the 1st and 2nd CV curves of Vo¨-PNVO are greatly different from the subsequent curves. Specifically, there are three pairs of redox peaks at 0.72/0.83, 0.56/0.70 and 0.34/0.56 V at beginning (Fig. 4a), indicating a multiple-step Zn^{2+} intercalation/de-intercalation reaction mechanism [44]. The almost vanished redox pair at around 1.10/1.28 V suggests that the redox reaction of V^{5+}/V^{4+} is weakened due to the introduction of oxygen vacancies in the shallow layer of Vo¨-PNVO, which corresponds to the emerge of new redox pair at 0.72/0.83 V [15]. When vanadium ion has an oxygen octahedron coordination, an oxygen vacancy would render a change in electronic structure, causing the further splitting or deviation of orbital energy and leading to a change of charge-discharge voltage [45]. In the 3rd and 4th cycles, only two obvious pairs of redox peaks at 0.72/0.87 and 0.46/0.56 V are remained without deviation. This phenomenon indicates that the redox reactions in Vo¨-PNVO become reversible from the 3rd cycle. As further compared in Table 1, the smaller voltage difference in the redox pairs of Vo¨-PNVO suggests lower polarization and faster electrochemical kinetics than NVO. Oxygen vacancies can reduce the polarization with positive charge by balancing the strain/stress from Zn^{2+} and Vo¨-PNVO. As the V^{4+} with partially unfilled 3*d* orbitals can capture and transfer electrons in redox reactions, the Zn-ion storage reaction kinetics would be catalyzed [17]. Thus, the number of *d* orbitals located at the conduction band bottom and the valence band top increases due to the introduced oxygen vacancies and V^{4+}, enhancing the electrical conductivity and catalyzing the electrochemical reactions in Vo¨-PNVO.

Table 1
The redox pairs and voltage differences in the 4th CV curves of Vo¨-PNVO and NVO.

Sample	Redox pairs (V)	Difference (V)
Vo¨-PNVO	0.46/0.56	0.12
	0.72/0.87	0.15
NVO	0.41/0.79	0.38
	0.50/0.88	0.38
	1.10/1.33	0.23

In the Galvanostatic charge-discharge (GCD) curves of the Vo¨-PNVO (Fig. S2b), all the charge/discharge voltage plateaus connect and form a long and tilting platform. The initial discharge specific capacity of Vo¨-PNVO is 355 mA h g^{-1} at 0.05 A g^{-1}, and the specific capacity remains 295, 290, 285 mA h g^{-1} in the following three cycles, in accordance with the CV curves. The detailed storage mechanism will be explored further explored later. The values of Vo¨-PNVO are higher than that of NVO (315, 277, 230, 213 mA h g^{-1} at 0.05 A g^{-1}). Moreover, Vo¨-PNVO exhibits superior rate capability with capacities of 256, 234, 228, 224, 221, 205 and 165 mA h g^{-1} at 0.1, 0.2, 0.4, 0.8, 1, 2 and 4 A g^{-1}, respectively, and the capacity almost recovers when the rate switches back to 0.05 A g^{-1} (Fig. 4b). Compared with NVO, the improved capacity and higher rate performance of Vo¨-PNVO are closely related to PEDOT and oxygen vacancies. Note that it has been reported that pure PEDOT plays a relatively small role in capacity contribution (24 mA h g^{-1} at 0.2 A g^{-1}, and even smaller) and poor cycling performance [38,46]. The main role of PEDOT is to create oxygen vacancies and to simultaneously form a conductive coating to improve the overall conductivity and protect the core [25]. Thus, oxygen vacancies should mainly contribute to the high capacity. The rate performance of Vo¨-PNVO in regards of fast charge transfer kinetics will be discussed next.

The high rate performance of Vo¨-PNVO is reflected by energy efficiency, which is important for practical applications. In Fig. 4c, the smaller hysteresis area of the GCD curve suggests Vo¨-PNVO a higher

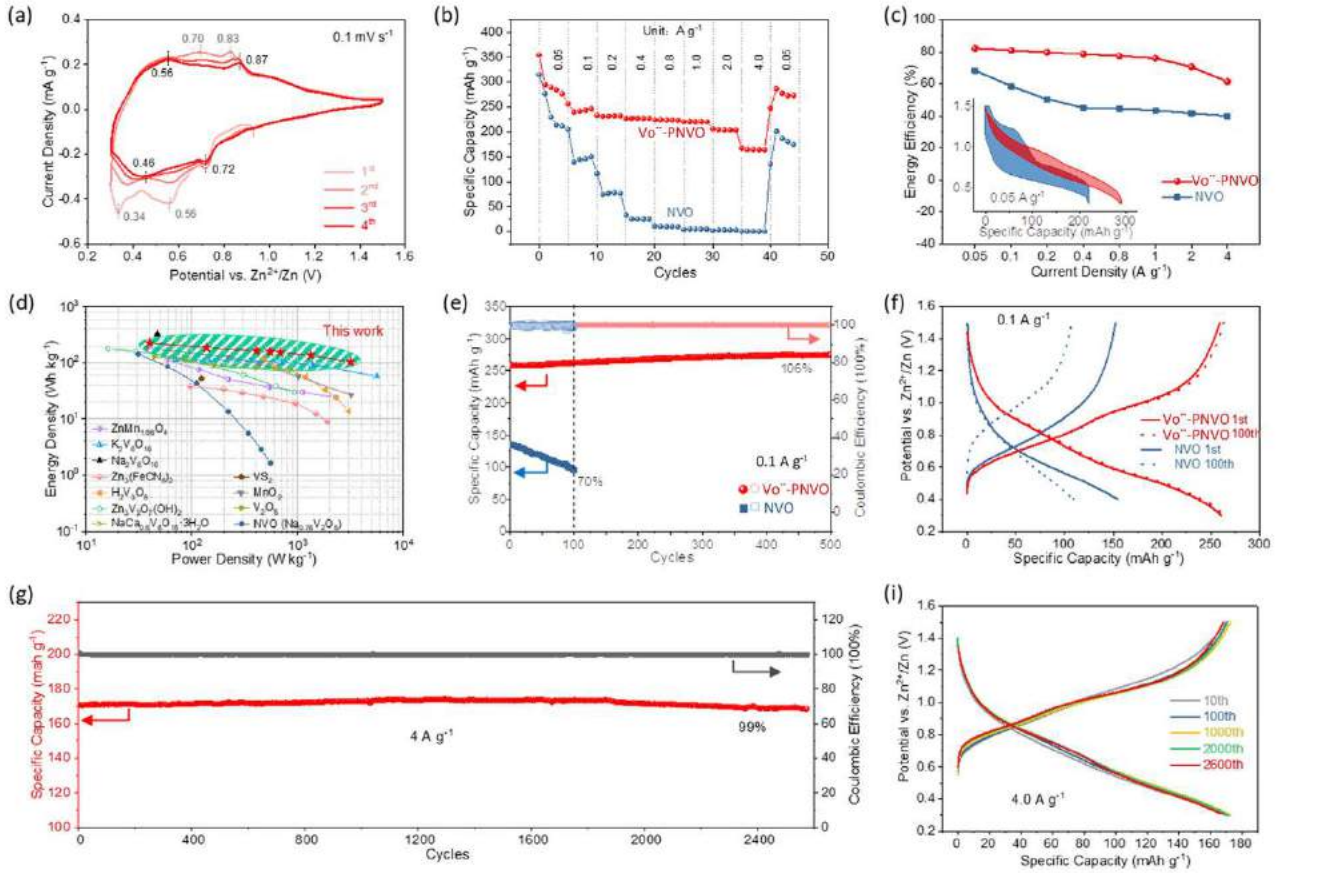

Fig. 4. (a) CV curves of Vo¨-PNVO collected at a sweep rate of 0.1 mV s^{-1}. The overlapping of the curves in the 3rd and 4th cycles means reaction reversibility in Vo¨-PNVO. (b) Rate performance of Vo¨-PNVO and NVO. (c) Energy efficiency of Vo¨-PNVO and NVO at various current densities. Inserted is voltage hysteresis of Vo¨-PNVO and NVO collected at 0.1 A g^{-1} in the 3rd cycle. Vo¨-PNVO displays smaller energy loss and higher energy efficiency than NVO. (d) Ragone plots of ZIBs based on Vo¨-PNVO, NVO and other cathode materials. (e) Cycling stability at 0.1 A g^{-1} and (f) corresponding GCD curves of Vo¨-PNVO and NVO. (g) Cycling stability of Vo¨-PNVO at 4 A g^{-1} and (h) corresponding GCD curves at different cycles.

energy efficiency and less energy loss than NVO. Calculated by the ratio of discharge and charge energy densities, the energy efficiency of Vo¨-PNVO is higher than that of NVO in different current densities (Fig. 4c). The enhanced energy efficiency of Vo¨-PNVO is ascribed to highly reversible Zn^{2+} intercalation/de-intercalation due to the introduction of PEDOT and oxygen vacancies. In addition, the Vo¨-PNVO-based ZIBs exhibit an energy-density/power-density of 228 W h kg^{-1}/40 W kg^{-1} and 105 W h kg^{-1}/3160 W kg^{-1} at 0.05 and 4.0 A g^{-1}, respectively, higher than NVO and the recently reported vanadium-, manganese- and Prussian blue-based ZIBs, as shown in Ragone plot in Fig. 4d.

Vo¨-PNVO also deliver excellent cycling performance. As shown in Fig. 4e, 106% capacity retention (275 mA h g^{-1}) and approximately 100% coulombic efficiency were obtained in Vo¨-PNVO after 500 cycles at a small current density of 0.1 A g^{-1}, while the capacity of NVO decays rapidly in 100 cycles (70% capacity retention). The well overlap of the 1st and 100th GCD curves of Vo¨-PNVO confirms the excellent cycling stability and high reversibility of Vo¨-PNVO (Fig. 4f). The nanocable structure of Vo¨-PNVO still remains well after 500 cycles, while the NVO structure was destroyed as small parts in 100 cycles, confirmed by the SEM and TEM images in Fig. S3a–d. Further tested at a large current density of 4 A g^{-1}, 99% of the initial capacity with approximately 100% coulombic efficiency is remained after 2600 cycles in Vo¨-PNVO (Fig. 4g). The corresponding GCD curves of the 10th, 100th, 1000th, 2000th and 2600th cycles at 4 A g^{-1} also overlap well (Fig. 4i). Moreover, the cycling performance of Vo¨-PNVO is superior to other electrode materials, such as $Na_{0.33}V_2O_5$ (93% retention after 1000 cycles) [8], $NH_4V_4O_{10}$ (70.3% retention after 2000 cycles) [47], $K_2V_8O_{21}$ (83% retention after 300 cycles) [18], V_2O_5@PEDOT nanosheet arrays (89% retention after 1000 cycles) [25], polyaniline intercalated V_2O_5 (87.5% retention after 600 cycles) [26] and polyaniline intercalated $V_2O_5{\cdot}nH_2O$ (80% retention after 800 cycles) [34]. Four possible factors are ascribed to the excellent cycling stability of Vo¨-PNVO: (1) Positively charged oxygen vacancies reduce the electrostatic interactions between Zn^{2+} and host to inhibit the structural collapse. Oxygen vacancies also provide void sites for fast electron reception/donation, and offer larger lattice distance for Zn^{2+} diffusion, significantly enhancing the kinetics and electrochemical stability of Vo¨-PNVO. (2) Conductive PEDOT coating may also help to improve overall conductivity as well as preserve the morphology integrity by preventing the dissolution of inner NVO from directly contacting the electrolyte [25,36,48–50]. (3) The structure stability is also related to the chemical bonds between PEDOT and NVO in Vo¨-PNVO. The robust connection renders PEDOT coating firmly attached in Vo¨-PNVO after 500 cycles (Fig. S3d), while the pure PEDOT shows serious capacity fade [38]. (4) The electrolyte selection of 3 M $Zn(CF_3SO_3)_2$ matters in electrochemical stability. Vo¨-PNVO shows better cycling performance in 3 M $Zn(CF_3SO_3)_2$ than in 3 M $ZnSO_4$ aqueous solution (76% retention after 2000 cycles, Fig. S3e).

3.3. Zn-storage mechanism exploration of Vo¨-PNVO

Various sweeping rates of CV curves were collected to investigate the reaction kinetics behind the enhanced rate performance of Vo¨-PNVO (Fig. 5a). The power-law relationship between peak currents (i) and

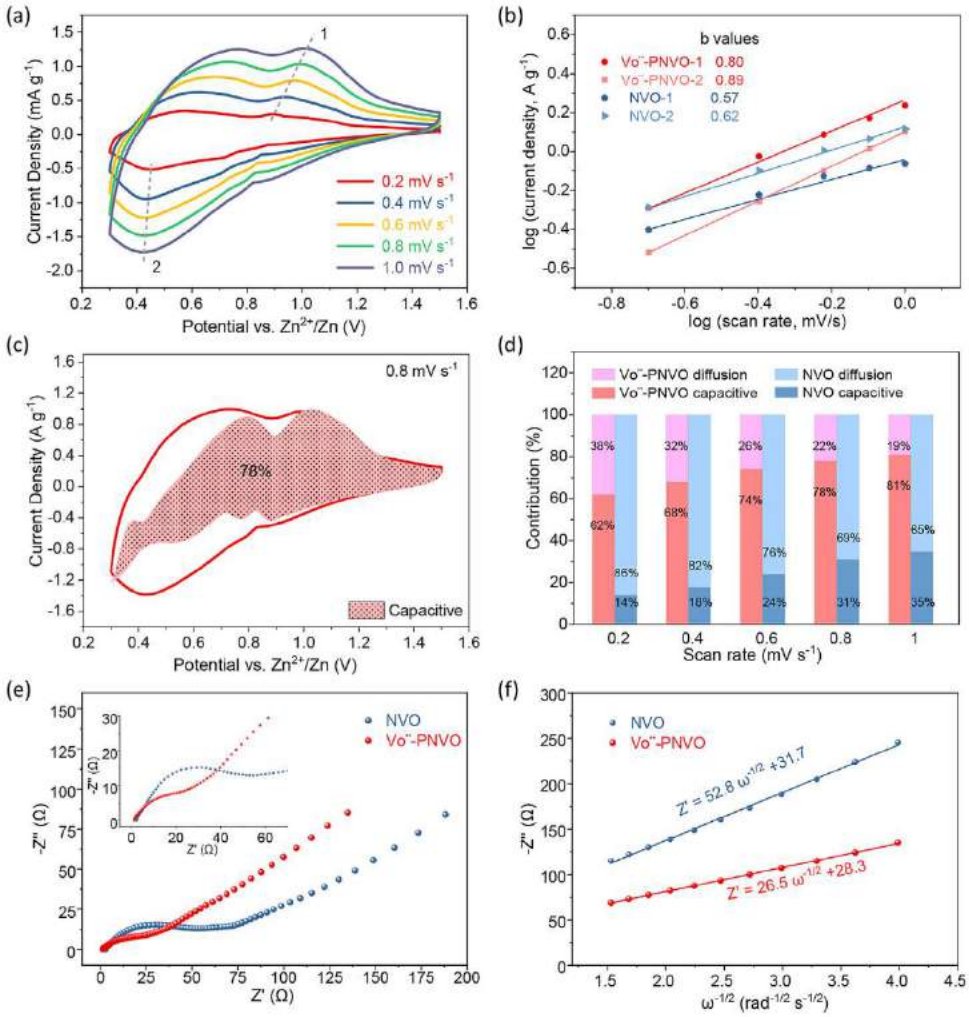

Fig. 5. (a) CV curves of Vo¨-PNVO at various sweep rates. (b) The relationship between peak currents and sweep rates, and corresponding b values. (c) Capacitive contribution in Vo¨-PNVO at 0.8 mV s^{-1}. (d) Diffusion and capacitive contributions of Vo¨-PNVO and NVO under different scan rates. (e) Nyquist plot of Vo¨-PNVO and NVO. (f) The relationship between the real part of impedance and low frequencies. The smaller slope of the linear tendency means faster ion diffusion in the electrochemical process.

sweep rates (v) is described as following:

$$i = av^b \tag{1}$$

where a and b are variables. A b value of 1 suggests a capacitive process and 0.5 is indicative of diffusion-controlled charge storage. With scan rates increased from 0.2 to 1 mV s^{-1}, the b values of peaks 1 and 2 in Vo¨-PNVO are 0.78 and 0.89, whereas these in NVO are 0.57 and 0.62, respectively (Fig. 5b). This indicates the electrochemical reactions in Vo¨-PNVO and NVO are controlled by both surface-controlled capacitance and diffusion-limited redox reactions, and more the capacitive behaviors in Vo¨-PNVO than in NVO at peak potentials. The capacitive and diffusion contribution at various scan rates can be obtained via the equation of

$$i(v) = k_1 v + k_2 v^{1/2} \tag{2}$$

where k_1 and k_2 are proportional to capacitance and diffusion contributions, respectively. A visual capacitive contribution of 78% in Vo¨-PNVO at 0.8 mV s^{-1} was shown in Fig. 5c. The capacitance contribution increases with sweep rate increased, and it is higher in Vo¨-PNVO than NVO (Fig. 5d). As the high rate performance and energy efficiency of Vo¨-PNVO are attributed to Zn^{2+} diffusion and capacitive behavior, the reasons can be summarized as following: (1) Oxygen vacancies can promote the capacitance-type charge storage with fast charge storage kinetics. Oxygen vacancies enable fast electron transfer with void sites to fast accept/donate electrons, and promote Zn^{2+} diffusion with expanded interplanar distance. (2) Conductive PEDOT enhances charge storage dynamics by enhancing electron transfer and shortening the charge transport distance. [36,48–50] (3) The electrolyte, namely, 3 M $Zn(CF_3SO_3)_2$, also relates to the Zn-storage capability of Vo¨-PNVO. When tested with 3 M $ZnSO_4$ aqueous solution as electrolyte, Vo¨-PNVO based ZIBs exhibit less satisfactory rate performance and stability than 3 M $Zn(CF_3SO_3)_2$ aqueous solution, although it is better than in NVO (Fig. S4a–e). $Zn(CF_3SO_3)_2$ electrolyte favors superior electrochemical properties due to its higher ionic conductivity and facilitated charge transfer, which probably because of the smaller charge density (compared with double-charge SO_4^{2-}) and weaker solvation of bulky $CF_3SO_3^-$ anions [4,51,52].

Galvanostatic intermittent titration technique (GITT) to conducted to analyze the interfacial charge-transfer kinetics of Vo¨-PNVO. As shown in Fig. S5a–c, the internal reaction resistance (RR) of Vo¨-PNVO (0~0.3 Ω g^{-1}) is much smaller than NVO (0.2~1.2 Ω g^{-1}). Moreover, the corresponding Zn^{2+} diffusion coefficient (D_{Zn}^{2+}) of Vo¨-PNVO is calculated between 10^{-14} and 10^{-13} cm^2 S^{-1}, higher than that of NVO from 10^{-15} to 10^{-14} cm^2 S^{-1}. The results suggest that Vo¨-PNVO has fast kinetics for better rate capability than NVO. Electrochemical impedance spectroscopy (EIS) was also used in Fig. 5e. The Nyquist plot consist of a semi-circle at the high-frequency region and a linear tail at low-frequency region, which are related to charge transfer resistance (R_{ct}) and ion diffusion. In Table 2, Vo¨-PNVO show a lower R_{ct} value (5.7 Ω) than NVO (25.6 Ω), suggesting faster charge transfer in Vo¨-PNVO. The D_{Zn}^{2+} values of Vo¨-PNVO and NVO are calculated through the relationship between low frequencies and the real part of impedance (Fig. 5f) [13]. Vo¨-PNVO present a larger D_{Zn}^{2+} of 3.5×10^{-14} cm^2 S^{-1} compared to that of 8.9×10^{-15} cm^2 S^{-1} in NVO. Consistent with GITT

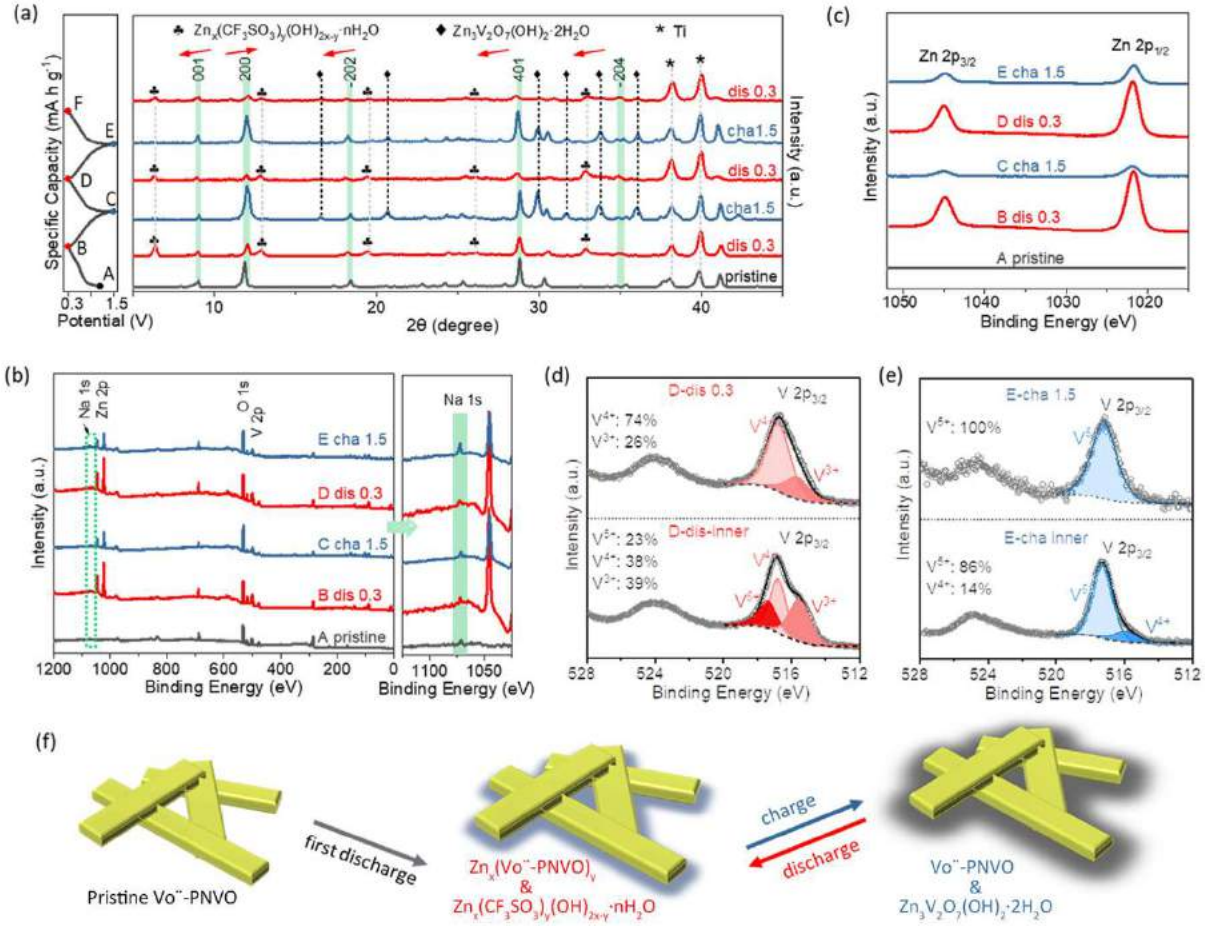

Fig. 6. *Ex-situ* of Vo¨-PNVO at different full discharge and charge states: (a) *ex-situ* XRD patterns, *ex-situ* XPS patterns of (b) full survey, (c) Na 1 s, (d) Zn 2p and (e) V2p spectra. (f) Illustration of the energy storage mechanism of Vo¨-PNVO.

Table 2
The *Rs*, *Rct* values and ion diffusion coefficient (D_{Zn}^{2+}) of Vo¨-PNVO and NVO obtained from the EIS spectra.

Sample	*Rs* (Ω)	*Rct* (Ω)	D_{Zn}^{2+} ($cm^2\ s^{-1}$)
Vo¨-PNVO	1.4	5.7	3.5×10^{-14}
NVO	2.6	25.6	8.9×10^{-15}

result, the lower R_{ct} value and higher D_{Zn}^{2+} in Vo¨-PNVO confirm the contributions of oxygen vacancies and PEDOT in electron transfer and ion diffusion (experimentally and theoretically discussed above). Thus, the resulted fast redox reactions and stable crystal structure endow the above high rate performance, energy efficiency and cycling stability of Vo¨-PNVO.

The Zn-ion storage mechanism of Vo¨-PNVO was studied by means of *ex-situ* XRD. The XRD patterns of full charge and discharge states in the initial three cycles are displayed in Fig. 6a. In the first full discharge state, the main (200) peak shifts slightly to a high angle from the pristine state, and the (001), (401), (−202) and (−204) peaks move to the low angle regions. The peak shifts suggest the (001) facet is enlarged from 9.72 Å to 9.92 Å, while the (200) and (−202) plane is contracted slightly, which is because Zn^{2+} intercalated into the structure interior and have electrostatic interaction with the host Vo¨-PNVO [47,53]. At the same time, new peaks (marked with club) located at 6.4°, 12.9°, 19.4°, 26.2°, and 32.8° emerge, matching well with the patterns of $Zn_x(CF_3SO_3)_y(OH)_{2x-y}{\cdot}nH_2O$ [51,54]. It is reported as the co-insertion mechanism of a proton and Zn^{2+}, where OH^- reacts with $Zn(CF_3SO_3)_2$ and $Zn_x(CF_3SO_3)_y(OH)_{2x-y}{\bullet}nH_2O$ forms on the surface of the electrode. [54,55] The proton insertion corresponds to the capacitive contributions from Eq. (2). Note that the insulating $Zn_x(CF_3SO_3)_y(OH)_{2x-y}{\bullet}nH_2O$ is undesirable as the battery internal resistance will be increased and the electrochemical reactions would be impeded with decreased active area. [54] Thus, the formation of $Zn_x(CF_3SO_3)_y(OH)_{2x-y}{\bullet}nH_2O$ should be mainly responsible for the capacity decay from 355 to 295 mA h g^{-1} in the first discharge process. In the following charge state, the $Zn_x(CF_3SO_3)_y(OH)_{2x-y}{\bullet}nH_2O$ phase disappears and Vo¨-PNVO peaks recover to original states, accompanied with another series of peaks belonging to $Zn_3V_2O_7(OH)_2{\bullet}2H_2O$ (JCPDS No.87-0417, marked with diamond) [26]. Then, the above two byproducts reversibly and alternately formed in the following charge and discharge states. The subsequently formed $Zn_3V_2O_7(OH)_2{\bullet}2H_2O$ probably shows certain electrochemical activity and contribute partially to the capacity by involving in the Zn^{2+} storage, which has been reported and will not be further investigated [26,47]. In brief, the byproducts of $Zn_x(CF_3SO_3)_y(OH)_{2x-y}{\bullet}nH_2O$ and $Zn_3V_2O_7(OH)_2{\bullet}2H_2O$ can explain the decay in the initial capacities (355, 295, 290 and 285 mA h g^{-1}), as well as the difference in the CV curves of Vo¨-PNVO. Note that, although the byproducts form, the main crystalline structure is still Vo¨-PNVO which deliver high rate performance and energy efficiency due to oxygen vacancies and PEDOT (discussed above).

The reaction mechanism of Vo¨-PNVO was further examined by *ex-situ* XPS measurements, as shown in Fig. 6b–d. Na 1 s is observed in both charge and discharge processes of Vo¨-PNVO (Fig. 6b). Zn 2p peaks observed in full charge states imply incomplete extraction of Zn^{2+} or new phase form (Fig. 6c). The peak gap between O 1 s and V $2p_{3/2}$ gets

larger in discharge states than in charge states (Table S1), and the V $2p_{3/2}$ spectra appear at lower energy regions at full discharge states than full charge states (Fig. S6a). The above result suggests more low vanadium valences in discharge states reduced along with the intercalation of Zn^{2+}. Thus, the V $2p_{3/2}$ spectra were deconvoluted to explore the vanadium oxidation states. In the discharge-charge process (Fig. S6b–d), the pristine V^{5+} and V^{4+} were reduced into V^{4+} and V^{3+} at discharge states and recovered to V^{5+} and V^{4+} at charge states. The stable discharge-state D and charge-state E electrodes were further investigated. The SEM images (Figu. S7a and b) show that there are flakes on the surface of discharge-state D electrode. Based on the XRD and the EDS results (Fig. S7c), these flakes should be $Zn_x(CF_3SO_3)_y(OH)_{2x-y}\bullet nH_2O$. Moreover, XPS V $2p_{3/2}$ spectra shows that there are V^{4+} and V^{3+} at the surface of discharge-state D electrode, while V^{5+}, V^{4+} and V^{3+} are collected when the D electrode was etched (Fig. 6d). This confirms that high valence vanadium was reduced with the Zn^{2+} intercalation. As XPS measurements focus on surface characterizations, the result also indicates the surface-layer location of oxygen vacancies in Vo¨-PNVO. The charge state E electrode present large $Zn_3V_2O_7(OH)_2\bullet 2H_2O$ sheets at the surface (SEM images in Fig. S7d and e), which are confirmed by EDS analysis in Figure S7f. In XPS V $2p_{3/2}$ spectra in Fig. 6e, only V^{5+} is detected (most likely comes from the $Zn_3V_2O_7(OH)_2\bullet 2H_2O$ at the surface), while V^{5+} along with a small amount of V^{4+} exist in inner part after surface etching. Based on the ex-situ XRD, XPS and SEM results, the possible redox reactions are illustrated in Fig. 6f: $Zn_x(CF_3SO_3)_y(OH)_{2x-y}\bullet nH_2O$ and $Zn_3V_2O_7(OH)_2\bullet 2H_2O$ reversibly and alternately formed in the discharge and charge states after the first discharge.

4. Conclusions

Oxygen-vacancy rich $Na_{0.76}V_6O_{15}$/PEDOT nanocables (Vo¨-PNVO) were synthesized as cathode materials for aqueous ZIBs. Both experimental results and DFT calculations elucidated that the bridge-oxygen sited oxygen vacancies in Vo¨-PNVO provide large interplanar distance, remarkably enhancing the electron transfer and Zn^{2+} diffusion and weaken the electrostatic interactions. With the synergistic effects of the oxygen vacancies and conductive PEDOT coating, Vo¨-PNVO based ZIBs deliver excellent performance with high energy conversion efficiency, high energy and high power, and excellent cycling stability (99% capacity retention over 2600 cycles). The results demonstrated that introducing oxygen vacancies is an effective strategy for high-performance ZIB cathodes. In addition, the mechanism study offers detailed information for better understanding of Zn^{2+} ion storage.

Declaration of Competing Interest

The authors declare that they have no known competing financial interests or personal relationships that could have appeared to influence the work reported in this paper

CRediT authorship contribution statement

Wenchao Bi: Conceptualization, Methodology, Software, Investigation, Writing – original draft, Writing – review & editing, Visualization. **Guohua Gao:** Software, Resources, Supervision, Writing – original draft, Funding acquisition. **Guangming Wu:** Resources, Supervision, Project administration, Funding acquisition. **M. Atif:** Resources. **MS AlSalhi:** Resources. **Guozhong Cao:** Resources, Supervision, Writing – review & editing, Visualization, Funding acquisition.

Acknowledgement

The authors are grateful for the financial support from National Natural Science Foundation of China (grant No. 51872204, No. 52072261, No. 22011540379), the National Key Research and Development Program of China (grant No. 2017YFA0204600), Shanghai Social Development Science and Technology Project (grant No. 20dz1201800), Shanghai Sailing Program (21YF1430900). This work is also supported by the National Science Foundation (1803256). The authors are grateful to the Deanship of Scientific Research, King Saud University for funding through Vice Deanship of Scientific Research Chairs.

Supplementary materials

Supplementary material associated with this article can be found, in the online version, at doi:10.1016/j.ensm.2021.05.003.

References

[1] D. Kundu, B.D. Adams, V. Duffort, S.H. Vajargah, L.F. Nazar, A high-capacity and long-life aqueous rechargeable zinc battery using a metal oxide intercalation cathode, Nat. Energy 1 (2016) 119.
[2] F. Wang, O. Borodin, T. Gao, X. Fan, W. Sun, F. Han, A. Faraone, J.A. Dura, K. Xu, C. Wang, Highly reversible zinc metal anode for aqueous batteries, Nat. Mater. 17 (2018) 543–549.
[3] P. Yu, Y. Zeng, H. Zhang, M. Yu, Y. Tong, X. Lu, Flexible Zn-ion batteries: recent progresses and challenges, Small 15 (2019) e1804760.
[4] N. Zhang, F. Cheng, J. Liu, L. Wang, X. Long, X. Liu, F. Li, J. Chen, Rechargeable aqueous zinc-manganese dioxide batteries with high energy and power densities, Nat. Commun. 8 (2017) 405.
[5] W. Sun, F. Wang, S. Hou, C. Yang, X. Fan, Z. Ma, T. Gao, F. Han, R. Hu, M. Zhu, C. Wang, Zn/Mn_{O2} battery chemistry with H^+ and Zn^{2+} coinsertion, J. Am. Chem. Soc. 139 (2017) 9775–9778.
[6] Y. Fu, Q. Wei, G. Zhang, X. Wang, J. Zhang, Y. Hu, D. Wang, L. Zuin, T. Zhou, Y. Wu, S. Sun, High-performance reversible aqueous Zn-ion battery based on porous MnOx nanorods coated by MOF-derived N-doped carbon, Adv. Energy Mater. 8 (2018) 1801445.
[7] F. Wan, L. Zhang, X. Dai, X. Wang, Z. Niu, J. Chen, Aqueous rechargeable zinc/sodium vanadate batteries with enhanced performance from simultaneous insertion of dual carriers, Nat. Commun. 9 (2018) 1656.
[8] P. He, G. Zhang, X. Liao, M. Yan, X. Xu, Q. An, J. Liu, L. Mai, Sodium ion stabilized vanadium oxide nanowire cathode for high-performance zinc-ion batteries, Adv. Energy Mater. 8 (2018) 1702463.
[9] Z. Li, T. Liu, R. Meng, L. Gao, Y. Zou, P. Peng, Y. Shao, X. Liang, Insights into the structure stability of prussian blue for aqueous zinc ion batteries, Energy Environ. Mater. 1 (2020) 1–6.
[10] C. Wang, S. Wei, S. Chen, D. Cao, L. Song, Delaminating vanadium carbides for zinc-ion storage: hydrate precipitation and H^+/Zn^{2+} co-action mechanism, Small Methods 3 (2019) 1900495.
[11] P. He, M. Yan, G. Zhang, R. Sun, L. Chen, Q. An, L. Mai, Layered VS2 nanosheet-based aqueous Zn ion battery cathode, Adv. Energy Mater. 7 (2017) 1601920.
[12] X. Jia, C. Liu, Z.G. Neale, J. Yang, G. Cao, Active materials for aqueous zinc ion batteries: synthesis, crystal structure, morphology, and electrochemistry, Chem. Rev. 120 (2020) 7795–7866.
[13] C. Liu, Z. Neale, J. Zheng, X. Jia, J. Huang, M. Yan, M. Tian, M. Wang, J. Yang, G. Cao, Expanded hydrated vanadate for high-performance aqueous zinc-ion batteries, Energy Environ. Sci. 12 (2019) 2273–2285.
[14] J. Ding, Z. Du, L. Gu, B. Li, L. Wang, S. Wang, Y. Gong, S. Yang, Ultrafast Zn^{2+} intercalation and deintercalation in vanadium dioxide, Adv. Mater. 30 (2018) 1800762.
[15] Z. Li, Y. Ren, L. Mo, C. Liu, K. Hsu, Y. Ding, X. Zhang, X. Li, L. Hu, D. Ji, G. Cao, Impacts of oxygen vacancies on zinc ion intercalation in VO_2, ACS Nano 14 (2020) 5581–5589.
[16] R. Manikandan, C.J. Raj, M. Rajesh, B.C. Kim, S. Park, K.H. Yu, Vanadium pentoxide with H_2O, K^+, and Na^+ spacer between layered nanostructures for high-performance symmetric electrochemical capacitors, Adv. Mater. Interfaces 5 (2018) 1800041.
[17] C. Liu, M. Tian, M. Wang, J. Zheng, S. Wang, M. Yan, Z. Wang, Z. Yin, J. Yang, G. Cao, Catalyzing zinc-ion intercalation in hydrated vanadates for aqueous zinc-ion batteries, J. Mater. Chem. A 8 (2020) 7713–7723.
[18] B. Tang, G. Fang, J. Zhou, L. Wang, Y. Lei, C. Wang, T. Lin, Y. Tang, S. Liang, Potassium vanadates with stable structure and fast ion diffusion channel as cathode for rechargeable aqueous zinc-ion batteries, Nano Energy 51 (2018) 579–587.
[19] J.Q. Zheng, C.F. Liu, M. Tian, X.X. Jia, E.P. Jahrman, G.T. Seidler, S.Q. Zhang, Y.Y. Liu, Y.F. Zhang, C.G. Meng, G.Z. Cao, Fast and reversible zinc ion intercalation in Al-ion modified hydrated vanadate, Nano Energy 70 (2020) 104519.
[20] M. Yan, P. He, Y. Chen, S. Wang, Q. Wei, K. Zhao, X. Xu, Q. An, Y. Shuang, Y. Shao, K.T. Mueller, L. Mai, J. Liu, J. Yang, Water-lubricated intercalation in $V_2O_5.nH_2O$ for high-capacity and high-rate aqueous rechargeable zinc batteries, Adv. Mater 30 (2018) 1703725.
[21] X. Guo, G. Fang, W. Zhang, J. Zhou, L. Shan, L. Wang, C. Wang, T. Lin, Y. Tang, S. Liang, Mechanistic insights of Zn^{2+} storage in sodium vanadates, Adv. Energy Mater. 8 (2018) 1801819.
[22] Q. Pang, C. Sun, Y. Yu, K. Zhao, Z. Zhang, P.M. Voyles, G. Chen, Y. Wei, X. Wang, $H_2V_3O_8$ nanowire/graphene electrodes for aqueous rechargeable zinc ion batteries with high rate capability and large capacity, Adv. Energy Mater. 8 (2018) 1800144.
[23] W. Yang, L. Dong, W. Yang, C. Xu, G. Shao, G. Wang, 3D oxygen-defective potassium vanadate/carbon nanoribbon networks as high-performance cathodes for aqueous zinc-ion batteries, Small Methods 4 (2019) 1900670.

[24] Y. Cai, F. Liu, Z. Luo, G. Fang, J. Zhou, A. Pan, S. Liang, Pilotaxitic $Na_{1.1}V_3O_{7.9}$ nanoribbons/graphene as high-performance sodium ion battery and aqueous zinc ion battery cathode, Energy Storage Mater. 13 (2018) 168–174.
[25] D. Xu, H. Wang, F. Li, Z. Guan, R. Wang, B. He, Y. Gong, X. Hu, Conformal conducting polymer shells on V_2O_5 nanosheet arrays as a high-rate and stable zinc-ion battery cathode, Adv. Mater. Interfaces 6 (2019) 1801506–1801514.
[26] J. Zeng, Z.H. Zhang, X.S. Guo, G.C. Li, A conjugated polyaniline and water co-intercalation strategy boosting zinc-ion storage performances for rose-like vanadium oxide architectures, J. Mater. Chem. A 7 (2019) 21079–21084.
[27] Y. Zeng, Z. Lai, Y. Han, H. Zhang, S. Xie, X. Lu, Oxygen-vacancy and surface modulation of ultrathin nickel cobaltite nanosheets as a high-energy cathode for advanced Zn-ion batteries, Adv. Mater. 30 (2018) 1802396.
[28] G. Kresse, J. Furthmuller, Efficiency of ab-initio total energy calculations for metals and semiconductors using a plane-wave basis set, Comp. Mater. Sci. 6 (1996) 15–50.
[29] J.P. Perdew, K. Burke, M. Ernzerhof, Generalized gradient approximation made simple, Phys. Rev. Lett. 77 (1996) 3865–3868.
[30] P.E. Blochl, Projector augmented-wave method, Phys. Rev. B 50 (1994) 17953–17979.
[31] G. Kresse, D. Joubert, From ultrasoft pseudopotentials to the projector augmented-wave method, Phys. Rev. B 59 (1999) 1758–1775.
[32] T. Mueller, G. Hautier, A. Jain, G. Ceder, Evaluation of tavorite-structured cathode materials for lithium-ion batteries using high-throughput computing, Chem. Mater. 23 (2011) 3854–3862.
[33] W. Bi, J. Wang, E.P. Jahrman, G.T. Seidler, G. Gao, G. Wu, G. Cao, Interface engineering V_2O_5 nanofibers for high-energy and durable supercapacitors, Small 15 (2019) e1901747.
[34] M. Wang, J. Zhang, L. Zhang, J. Li, W. Wang, Z. Yang, L. Zhang, Y. Wang, J. Chen, Y. Huang, D. Mitlin, X. Li, Graphene-like vanadium oxygen hydrate (VOH) nanosheets intercalated and exfoliated by polyaniline (PANI) for aqueous zinc-ion batteries (ZIBs), ACS Appl. Mater. Interfaces 12 (2020) 31564–31574.
[35] H. Wu, G. Yu, L. Pan, N. Liu, M.T. McDowell, Z. Bao, Y. Cui, Stable Li-ion battery anodes by in-situ polymerization of conducting hydrogel to conformally coat silicon nanoparticles, Nat. Commun. 4 (2013) 1943.
[36] W. Bi, Y. Wu, C. Liu, J. Wang, Y. Du, G. Gao, G. Wu, G. Cao, Gradient oxygen vacancies in V_2O_5/PEDOT nanocables for high-performance supercapacitors, ACS Appl. Energy Mater. 2 (2018) 668–677.
[37] K. Zhu, T. Wu, K. Huang, $NaCa_{0.6}V_6O_{16}\bullet 3H_2O$ as an ultra-stable cathode for Zn-ion batteries: the roles of pre-inserted dual-cations and structural water in V_3O_8 layer, Adv. Energy Mater. 9 (2019) 1901968.
[38] D. Bin, W. Huo, Y. Yuan, J. Huang, Y. Liu, Y. Zhang, F. Dong, Y. Wang, Y. Xia, Organic-inorganic-induced polymer intercalation into layered composites for aqueous zinc-ion battery, Chem 6 (2020) 968–984.
[39] X. Zhao, M. Dong, J. Zhang, Y. Li, Q. Zhang, Vapor-phase polymerization of poly(3, 4-ethylenedioxythiophene) nanofibers on carbon cloth as electrodes for flexible supercapacitors, Nanotechnology 27 (2016) 385705.
[40] W. Bi, E.P. Jahrman, G.T. Seidler, J. Wang, G. Gao, G. Wu, M. Atif, M.S. AlSalhi, G. Cao, Tailoring energy and power density through controlling the concentration of oxygen vacancies in V_2O_5/PEDOT nanocable-based supercapacitors, ACS Appl. Energy Mater. 11 (2019) 16647–16655.
[41] C.X. Guo, G. Yilmaz, S. Chen, S. Chen, X. Lu, Hierarchical nanocomposite composed of layered V_2O_5/PEDOT/MnO_2 nanosheets for high-performance asymmetric supercapacitors, Nano Energy 12 (2015) 76–87.
[42] J. Zhang, H. Yang, G. Shen, P. Cheng, J. Zhang, S. Guo, Reduction of graphene oxide via L-ascorbic acid, Chem. Commun. 46 (2010) 1112–1114.
[43] H. Xu, C. Cheng, S. Chu, X. Zhang, J. Wu, L. Zhang, S. Guo, H. Zhou, Anion–cation synergetic contribution to high capacity, structurally stable cathode materials for sodium-ion batteries, Adv. Funct. Mater. 30 (2020) 202005164.
[44] D. Chao, X. Xia, J. Liu, Z. Fan, C.F. Ng, J. Lin, H. Zhang, Z.X. Shen, H.J. Fan, A V_2O_5/conductive-polymer core/shell nanobelt array on three-dimensional graphite foam: a high-rate, ultrastable, and freestanding cathode for lithium-ion batteries, Adv. Mater. 26 (2014) 5794–5800.
[45] C. Liu, Z.G. Neale, G. Cao, Understanding electrochemical potentials of cathode materials in rechargeable batteries, Mater. Today 19 (2016) 109–123.
[46] L. Ma, X. Wang, J. Sun, A strategy associated with conductive binder and 3D current collector for aqueous zinc-ion batteries with high mass loading, J. Electroanal. Chem 873 (2020) 114395.
[47] B. Tang, J. Zhou, G. Fang, F. Liu, C. Zhu, C. Wang, A. Pan, S. Liang, Engineering the interplanar spacing of ammonium vanadates as a high-performance aqueous zinc-ion battery cathode, J. Mater. Chem. A 7 (2019) 940–945.
[48] S.G. Im, D Kusters, W. Choi, S.H. Baxamusa, M.C.M. van de Sanden, K.K. Gleason, Conformal coverage of poly(3,4-ethylenedioxythiophene) films with tunable nanoporosity via oxidative chemical vapor deposition, ACS Nano 2 (2008) 1959–1967.
[49] H.T. Tan, X.R. Rui, H. Yu, W. Liu, Z.X. Chen, H.H. Hng, Q. Yan, Aqueous-based chemical route toward ambient preparation of multicomponent core_shell nanotubes, ACS Nano 8 (2014) 4004–4014.
[50] Y. Zeng, Y. Han, Y. Zhao, Y. Zeng, M. Yu, Y. Liu, H. Tang, Y. Tong, X. Lu, Advanced Ti-doped Fe_2O_3@PEDOT core/shell anode for high-energy asymmetric supercapacitors, Adv. Energy Mater. 5 (2015) 1402176.
[51] L. Wang, K.W. Huang, J. Chen, J. Zheng, Ultralong cycle stability of aqueous zinc-ion batteries with zinc vanadium oxide cathodes, Sci. Adv. 5 (2019) eaax4279.
[52] C. Xia, J. Guo, Y. Lei, H. Liang, C. Zhao, H.N. Alshareef, Rechargeable aqueous zinc-ion battery based on porous framework zinc pyrovanadate intercalation cathode, Adv. Mater. 30 (2018).
[53] M. Yan, P. He, Y. Chen, S. Wang, Q. Wei, K. Zhao, X. Xu, Q. An, Y. Shuang, Y. Shao, K.T. Mueller, L. Mai, J. Liu, J. Yang, Water-lubricated intercalation in $V_2O_5{\cdot}nH_2O$ for high-capacity and high-rate aqueous rechargeable zinc batteries, Adv. Mater. 30 (2018) 1703725.
[54] J. Guo, J. Ming, Y.J. Lei, W.L. Zhang, C. Xia, Y. Cui, H.N. Alshareef, Artificial solid electrolyte interphase for suppressing surface reactions and cathode dissolution in aqueous zinc ion batteries, ACS Energy Lett. 4 (2019) 2776–2781.
[55] N. Liu, X. Wu, L. Fan, S. Gong, Z. Guo, A. Chen, C. Zhao, Y. Mao, N. Zhang, K. Sun, Intercalation pseudocapacitive Zn(2+) storage with hydrated vanadium dioxide toward ultrahigh rate performance, Adv. Mater. 32 (2020) e1908420.